Amino hydroxyapatite/chitosan hybrids reticulated with glutaraldehyde at different pH values and their use for diclofenac removal

M.B.B. Pereira, D.B. França, Rafael Araújo, Edson Silva Filho, Baptiste Rigaud, M.G. Fonseca, Maguy Jaber

Amino hydroxyapatite/chitosan hybrids reticulated with glutaraldehyde at different pH values and their use for diclofenac removal

M.B.B. Pereira[a,b], D.B. França[a,b], Rafael C. Araújo[a,b], Edson C. Silva Filho[c], Baptiste Rigaud[d], M.G. Fonseca[a,b*], Maguy Jaber[d]

[a]*Universidade Federal da Paraíba, Cidade Universitária, 58051-085, João Pessoa, PB, Brazil.*

[b]*Núcleo de Pesquisa e Extensão, Laboratório de Combustíveis e Materiais (NPE – LACOM).*

[c]*Laboratório Interdisciplinar de Materiais Avançados (LIMAV), Centro de Tecnologia, Universidade Federal do Piauí, Teresina, Piaui, Brazil, 64064-260.*

[d]*Sorbonne Université, Laboratoire d'Archéologie Moléculaire et Structurale, CNRS UMR 8220, UPMC – Tour 23, 3ème étage, couloir 23-33, BP 225, 4 place Jussieu, 75005 Paris, France.*

*Phone/Fax: +55 83 3216-7433

email: mgardennia@quimica.ufpb.br

Highlights

- Amino hydroxyapatite/chitosan/glutaraldehyde hybrids were synthetized
- The influence of pH on crosslinking was investigated.
- Hybrids were characterized for structural, thermal and morphologic techniques.
- Hybrids adsorbed diclofenac from aqueous solution at pH 6.
- High drug adsorption (125.0 mg mg g^{-1}) was obtained for hybrid obtained at pH 3.

ABSTRACT

Diclofenac sodium (DS) is an emergent pollutant and among methods investigated for its removal, adsorption is an appropriated technique. Hydroxyapatite (HA) and chitosan (CS) are biomaterials often used for adsorption. However, both biomaterials are limited due their chemical stability in acidic medium; furthermore, pure HA has poor interaction with diclofenac. Amino bioadsorbents can adsorb DS by different mechanism. In this work, hydroxyapatite was initially organofunctionalized with 3-aminopropyltrimethoxysilane and further used to obtain amino hydroxyapatite/chitosan hybrids by crosslinking with glutaraldehyde. The efficiency of the crosslinking reaction at pH 3, 4, 5 and 6 was investigated at room temperature over 10 min. X-ray diffraction patterns indicated the preservation of the hydroxyapatite phase under all pH conditions. Based on control reaction of the amino hydroxyapatite with glutaraldehyde and its further reduction in sodium borohydride, the formation of C=N moieties was highlighted as the main mechanism of interaction between the aldehyde and amino groups. Therefore, crosslinking with glutaraldehyde was evaluated by infrared, Raman spectroscopy and ^{13}C NMR and suggested contributions of imine formation and also hydrogen bonding. Higher crosslinking was achieved at pH 3 and 4 than at pH 5 and 6, as indicated by CHN analysis and thermogravimetry. Alterations in the surface of the samples were showed by scanning electron microscopy. Rapid diclofenac removal occurred at 30 and 15 min for amino-hydroxyapatite/glutaraldehyde/chitosan obtained at pH 3 and pH 4, respectively. In the equilibrium study, the hybrid obtained at pH 3 achieved better adsorption capacity of 125 mg g^{-1} (99% drug removal). Synergism between amino hydroxyapatite and CS crosslinked by glutaraldehyde was demonstrated, and both hybrids obtained at lower pH (3 and 4) presented high efficiency in DS removal from aqueous solution.

Keywords: Amino hydroxyapatite; chitosan; crosslinking; diclofenac; adsorption

1. Introduction

The increased use of diverse classes of medicines is a growing requirement to ensure a better quality of life for the population (Basheer, 2018; Triebskorn et al., 2015).

The consequently enlarged volume of pharmaceutical waste from industries, hospitals and homes is reported to cause disruption in water resources by damaging the quality of drinking water (Yan et al. 2019; Riegger et al. 2018; De Oliveira et al. 2017). Pharmaceutical residues are considered emerging pollutants, and diverse types of these residues have been detected in water, including anti-inflammatories and antibiotics (Bonnefille, Gomez, Courant, Escande, & Fenet, 2018; Sousa, Ribeiro, Barbosa, Pereira, & Silva, 2018).

Among pharmaceutical compounds, diclofenac sodium (DS) is one of the main drugs detected in water around the world (Acuña et al., 2015; Park & Lee, 2018; Sathishkumar et al., 2020). It is classified as a nonsteroidal anti-inflammatory drug and is indicated in the relief of all grades of pain and inflammation associated with a wide range of conditions, including arthritic conditions, acute musculoskeletal disorders and other painful conditions resulting from trauma (Lonappan, Rouissi, Kaur, Verma, & Surampalli, 2017; Sathishkumar et al., 2020). Due to its important applications, DS is the twelfth most widely used generic drug in the world. As a result, DS is an important emerging pollutant that is difficult to remove from water (Lessa, Nunes, & Fajardo, 2018; Soares, Fernandes, Sacramento, Trindade, & Daniel-da-silva, 2019).

Different processes are used for the treatment of polluted water, e.g., chemical precipitation, coagulation-flocculation, ionic exchange and adsorption (Lu & Astruc, 2018). Among these processes, adsorption is widely applied, and biosorbents based on natural and sustainable resources are effective in the removal of pharmaceutical

pollutants. In this field, biosorbents obtained from biopolymers are particularly promising (Hu et al., 2019).

Chitosan (CS) stands out as an excellent biosorbent due to its structure, which consists of N-acetyl-D-glucosamine and D-glucosamine units with free amino and hydroxyl groups that are highly reactive and capable of interacting with various pollutant molecules, such as drugs (Shariatinia & Jalali, 2018; Yang, Li, Huang, Yang, & Li, 2016). In addition, this biopolymer is biodegradable, nontoxic, and derived from a natural and economical raw material obtained mainly from the deacetylation of chitin (Vakili et al., 2018).

CS also interacts with inorganic matrices, resulting in composites with improved properties such as enhanced chemical stability (Chatterjee et al., 2018). Among inorganic matrices, calcium phosphates, such as hydroxyapatite, have been applied as good candidates to form new hybrids for environmental applications (Shi, Lv, Wu, & Hou, 2017). Hydroxyapatite ($Ca_{10}(PO_4)_6(OH)_2$) is used as an adsorbent due to its biocompatibility and its production in large scale by using green, economic and easy processes (Wang et al., 2017). Hydroxyapatite (HA) has reactive functional groups, Ca-OH and P-OH (Harja & Ciobanu, 2018; Hassan & Hrdina, 2018), that allow interactions with several neutral, cationic and anionic species by hydrogen bonding and ion exchange. The adsorptive potential of the HA is improved through chemical modification with biopolymers, among which chitosan is the most investigated polymer for the formation of composites and nanocomposites. CS is used due many actives groups for reaction and adsorption (NH_2 and OH), that are viable to large pollutant removals. Furthermore, like HA, CS is also biocompatible, easily manufactured and also presents possibility to alter its physical texture for use as beads, films and powders that are interesting properties for many applications, including adsorption. The

combination of CS with other substrates at the molecular level can improve its use in environmental remediation (Chatterjee et al., 2018; Vakili et al., 2014).

Therefore, pure HA/CS composites have been described in the literature (Rogina et al., 2017; Shi et al., 2017) with tentative to describe the interactions beween both components. (Y. Li, Liu, Zheng, & Xu, 2013; Sanchez et al., 2018; Sun, Shi, Wang, & Li, 2017; Zima, 2018).

In this work, covalent chemical bonding through crosslinking formation between amino apatite and CS was used to obtain a more effective adsorbent for DS removal. Among the crosslink agents, glutaraldehyde is one of the most widely investigated bifunctional agents at pH 6 for the formation of C=N bonds (Ciaccia & Di Stefano, 2015; Lal, Arora, & Sharma, 2016). In this study for the first time, the influence of the pH on hybrid formation was systematically investigated and the formation of the hybrids was evidenced by structural, thermal and morphological techniques.

Therefore, the aims of this work were to obtain new hybrid bio adsorbents based on amino hydroxyapatite/glutaraldehyde/chitosan at different pH values. The new hybrids were applied to DS removal from aqueous solutions under varied experimental conditions, including the pH, mass of the adsorbent, time and initial drug concentration. The isotherm results were fitted with kinetic and equilibrium models and the interactions between the hybrids and the drug were evaluated.

2. Experimental

2.1 Chemicals

All chemicals were supplied by Sigma Aldrich and used without further purification.

For the preparation of HA, calcium chlorite, ammonium phosphate and NaOH were used. Chitosan with an average molecular weight of 190-310 kD and 78% deacetylation degree, glutaraldehyde (Glu, 25%), 3-aminopropyltrimethoxysilane, acetic acid and ammonium hydroxide were used for preparing the hybrids. In the adsorption experiments, diclofenac sodium (CAS 15307-79-6, $C_{14}H_{10}Cl_2NNaO_2$, pKa 4.1) was used.

2.2 Synthesis of silylated hydroxyapatite/chitosan reticulated with glutaraldehyde

Initially, the precursor HA was obtained through a coprecipitation (Silva, Alves, dos Santos, Fonseca, & Jaber, 2017). Briefly, 0.033 mol of calcium chloride and 0.056 mol of ammonium phosphate were mixed in an aqueous solution at pH 10.

The silylation of HA was performed under N_2 atmosphere. First, 3.0 g of HA was reacted with 2.5 mL of 3-aminopropyltrimethoxysilane for 72 h in toluene under reflux. The solid, HA-NH_2, was recovered after filtration and washing with ethanol and water until the pH was neutral and dried at 120 °C.

Crosslinking was performed by reacting 1.0 g of the silylated HA-NH_2 and 50 mL of a 2.5% Glu solution adjusted to pH 3, 4, 5 or 6 with 1% acetic acid or 1 mol L^{-1} NaOH monitored in a digital pH meter (Digimed) (See Supplementary Material Figure SM1). The system was reacted for 10 min with vigorous stirring at room temperature. The solid changed from white to reddish-brown. CS solution (50 mL) was prepared by

dissolving 200 mg of the biopolymer in 1% acetic acid (pH 3, 4, 5 or 6, previously adjusted) and was added to the system. The reaction was maintained for another 20 min and monitored as described. After the addition of the CS solution, the mixture quickly showed gelification (~ 5 min) and became dark reddish-brown, suggesting the formation of the (-C=N-) chromophore (Riegger et al., 2018). The resulting uniform gel was centrifuged, washed in distilled water and dried at 60 °C. All preparations occurred at rigorous pH control at values of 3, 4, 5 or 6 monitored in digital pH meter. Essentially, the pH is a fundamental parameter, as it is important to ensure the protonation of the carbonyl groups and to keep the primary amino groups deprotonated (Antony, Arun, & Manickam, 2019; Poon, Wilson, & Headley, 2014).

The obtained hybrids were denoted as HA-NH_2/CS-3, HA-NH_2/CS-4, HA-NH_2/CS-5 and HA-NH_2/CS-6, that are related to precursors and the pH used in the synthesis.

As control, hybrid obtained without glutaraldehyde was also prepared at pH 5, aiming to investigate possible interactions in absence of reticulation agent.

A second control was synthetized by reaction of the silylated HA with glutaraldehyde without biopolymer at pH 5 at the same conditions and was named as HA-NH_2/Glu.

HA-NH_2/Glu also reacted with sodium borohydride in aqueous solutions for 4 h following previous method (Fonseca & Airoldi, 1999). This reaction was used as a third control to reduce C=N moieties previously formed.

2.3 Batch adsorption procedure

In general, the experiments were carried out in a temperature-controlled Tecnal TE-4200 shaker incubator at a shaking rate of 200 rpm. The experiments were performed starting with 50 mg of each hybrid and 25 mL of a 100 mg L^{-1} drug solution at controlled pH at 25 ºC for 24 h. The influence of the pH on DS removal was monitored by using drug solution at 100 mg L^{-1} and 50 mg of the adsorbent at fixed initial pH in the range of 6 to 12 for 6 h. pH below 6 was not investigated due to the precipitation of the drug at lower pH than 6. After adsorption, supernatant was separated by centrifugation. The amounts of drug in both the initial and supernatant solutions were quantified at 273 nm by using UV-Vis spectrometry with a TCC-240 model Shimadzu spectrometer. The amount of adsorbed drug was calculated by equation 1:

$$q = \frac{(C_i - C_e)V}{m} \qquad (1)$$

where C_i and C_e are the initial and residual drug concentrations, respectively; V is the volume of the drug solution; and m is the mass of the adsorbent.

The influences of the dose of the adsorbent, time and initial drug concentrations were also evaluated. All tests were performed in triplicate, and the average value was obtained by statistical analysis.

2.4 Kinetic and equilibrium models

The experimental data were fitted to kinetic and equilibrium models (see Supplementary material SI1).

2.5 Characterizations

X-ray diffraction patterns were recorded using a XD3A Shimadzu powder X-ray diffractometer with CuK_{α} radiation (λ= 0.15406 nm). The XRD patterns were acquired between 3 and 80° (2θ) with a scanning rate of 0.02° min^{-1} at room temperature, and the diffractometer operated at 40 kV and 30 mA.

Fourier transform infrared spectroscopy (FTIR) was performed on a Bomem MB-series MB spectrometer. The samples were prepared in KBr pellets with a concentration of 2%. FT-IR spectra were recorded in the middle IR region (4000-400 cm^{-1}) with a resolution of 4 cm^{-1} and 30 scans.

FT-Raman spectra were recorded on a Bruker RFS/100S model spectrometer fitted with a liquid nitrogen-cooled Ge detector. The 1064 nm line of a Nd^{3+}/YAG laser was used at an incident power output of 100 mW. The spectral resolution was 4 cm^{-1}.

TG measurements were carried out by a TG I/1600 HT simultaneous thermal analyzer under a nitrogen flow of 50 mL min^{-1} with 10 mg samples and a heating rate of 10 ºC min^{-1} from room temperature to 1000 ºC.

The degree of organofunctionalization was determined based on CHN elemental analysis, which was performed on a Perkin-Elmer PE-2400 microelemental analyzer.

Zeta potential (ζ) was acquired on a Zetasizer Nano Zs ZS90 model instrument (Malvern Instruments) for isoelectric titration through pH titration. The pH of the solutions was adjusted with 0.100 mol L^{-1} NaOH or 0.500 mol L^{-1} HNO_3.

UV-Vis solid-state spectra were obtained on a Shimadzu spectrometer model UV-2550 in the range of 200-900 nm.

The morphology of the samples was monitored by scanning electron microscopy performed in an FEI Quanta FEG 250 microscope at an accelerating voltage of 1-30 kV. Samples were fixed on carbon tape and coated with Au in a Quorum model Q150R sputter-coater for 35 s at 20 mA by a plasma generated under an argon atmosphere.

Specific surface area was determined by using BET equation in the same conditions of previous work (Silva et al., 2017). Samples were degassed at 100 ^{o}C prior to analysis.

3. Results and Discussion

3.1 Characterization

3.1.1 X-ray diffraction

The X-ray pattern of the HA (Fig. 1a) exhibited typical reflections at 2θ of 25.8, 29.9, 34.0, 39.9, 46.7 and 49.4° indexed to the (002), (300), (202), (130), (222) and (213) diffraction planes, respectively, in agreement with ICDD 09.3204 (Dorozhkin, 2012; Szcześ, Hołysz, & Chibowski, 2017). After reaction of HA with the silane, the main reflections were still observed, suggesting the maintenance of the HA phase after silylation (Fig. 1b).

The XRD patterns of chitosan presented two broad peaks at 2θ of 9.8° and 19.9°, which were assigned to hydrated regions and coexisting ordered and amorphous regions, respectively (Bayrak, Demirtaş, & Gümüşderelioğl, 2017; Shi et al., 2017).

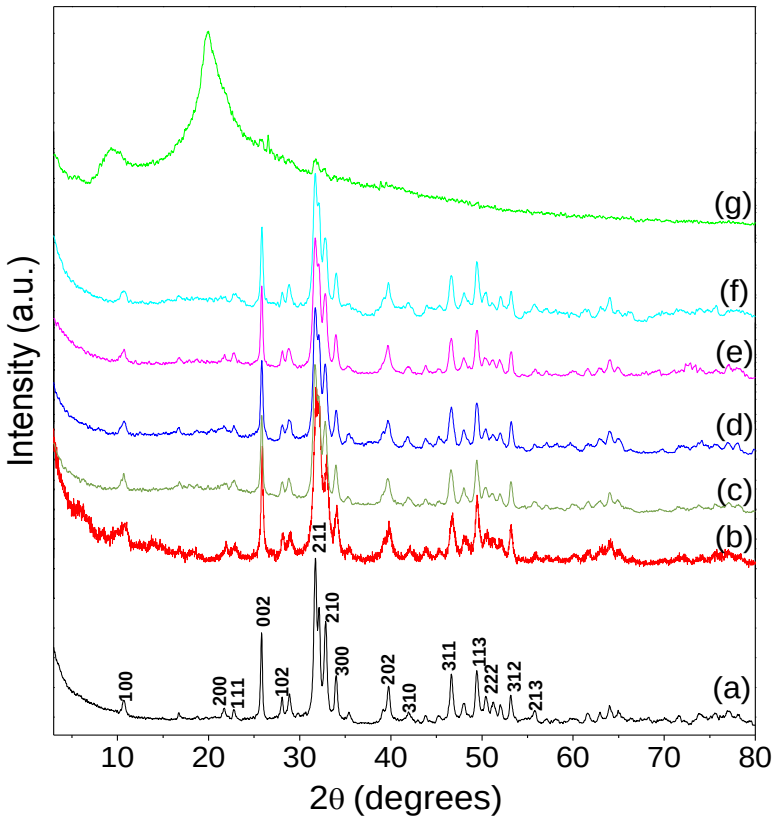

277

278

279 **Figure 1.** X-ray diffractograms for (a) HA, (b) HA-NH_2, (c) HA-NH_2/CS-3, (d) HA-
280 NH_2/CS-4, (e) HA-NH_2/CS-5, (f) HA-NH_2/CS-6 and (g) CS.

281

282 The crosslinking reaction promotes the interaction between the silylated HA and
283 chitosan mediated by a bifunctional agent on the molecular scale to generate an
284 inorganic-organic hybrid (Huang et al., 2011). Therefore, the XRD patterns of the
285 hybrids predominantly showed characteristics of the inorganic phase at the used w/w
286 proportion of each phase (15% chitosan and 85% HA-NH_2) for all pH values. No
287 indication of amorphous phases was observed in the XRD patterns even at pH 3.
288 Therefore, the crosslinking of calcium phosphate and chitosan did not alter the
289 inorganic phase in the pH range from 3 to 6.

290 The present results were different from those obtained with a pure
291 HA/Glu/chitosan composite (Y. Li et al., 2013), where the authors observed CS as

preponderant phase in XRD, even for composites prepared with 65% HA by weight in relation to the polymer/HA proportion and different conditions of synthesis including long time of reaction, at least 18 h.

3.1.2 Vibrational spectroscopy

Initially FTIR spectra of the controls obtained for pure HA-NH_2, HA-NH_2/Glu and HA-NH_2/Glu/reduced were prior analyzed. The FTIR spectrum of the HA showed bands at 3571 cm^{-1}, assigned to O-H stretching of the P-OH group, and at 3443 cm^{-1} and 1640 cm^{-1} due to OH stretching and bending of water, respectively (Manatunga, De Silva, De Silva, & Ratnaweera, 2016) . Typical bands of the asymmetric and symmetric stretching of PO_4^{3-} and P-O(H) in HPO_4^{-2} were observed at 1095-905 cm^{-1} and 870 cm^{-1}, respectively. Absorptions corresponding to deformations of these same groups were present at 599 and 560 cm^{-1}, respectively (Elliott J.C., 1994; Lin-Vien, Colthup, Fateley, & Grasselli, 1991; Nazeer, Yilgör, & Yilgör, 2017; Rogina et al., 2017; Silva et al., 2017). The organofunctionzalization of the HA through silylation resulted in new bands in the spectrum of HA-NH_2 at 2920 and 2850 cm^{-1} assigned to C-H asymmetric and symmetric stretching and at 1558 cm^{-1} assigned to NH_2 deformation. After reaction with glutaraldeyde, a broad band centered at 1655 cm^{-1} was maintained but a new band at 1330 cm^{-1} was assigned to =C-H deformation. Any alteration in bands associated to OH structural and PO_4^{3-} was observed. After reaction of the HA-NH_2/Glu with sodium borohydride, the band associated to =C-H deformation disappeared of the spectrum. The result is consistent with the reaction of primary amine moieties on silylated HA with aldehyde resulting formation of imine, and further reduction of previous imine, resulted

316 in a formation of secondary amine. The sequence of reactions was highlighted based on
317 infrared spectrum by the absence of typical =C-H after imine reduction.

318 For chitosan, a characteristic broad band centered at 3430 cm^{-1} was assigned to
319 O-H and N-H stretching of free hydroxyl and amino groups and was also related to
320 hydrogen bonding in the polymer (Modrzejewska et al. 2015; Salehi, Daraei and Arabi
321 Shamsabadi 2016; Venkatesan et al. 2016). A C-H stretching was observed in the 2935
322 -2870 cm^{-1} region. Additional bands at 1661 cm^{-1} were attributed to C=O stretching of
323 the amide, vibrations of the NH_2 group and deformation of water (Kyzas, Bikiaris and
324 Lazaridis 2008). The NH_2 deformation peak normally appears at 1577 cm^{-1}; however, it
325 overlaps with the amide II band near 1580 cm^{-1}. Therefore, the absorption at 1424 cm^{-1}
326 was assigned to the amide II band. Other absorption peaks were observed at 1150 cm^{-1},
327 due to C-O-C asymmetric stretching, and at 1080 and 1030 cm^{-1}, attributable to CO
328 stretching. This set of absorption peaks was associated with the chitosan structure (Jó et
329 al. 2017; Deepthi et al. 2016; Leceta et al. 2013).

330 For pure HA/CS hybrid obtained without glutaraldeyde, infrared spectrum
331 presented the band at 1640 cm^{-1}, assigned to N-H bending of the CS and also OH
332 deformation of water, which shifted for lower wavenumber compared to the initial band
333 of CS at 1664 cm^{-1}. Any alteration in the position in the OH stretching of the structural
334 hydroxyl of the HA (band at 3571 cm^{-1}) was observed as displayed in Table SM1 and
335 only N-H deformation at 1550 cm^{-1} was detected. Bands of phosphate occurs at same
336 region of C-O-C asymmetric stretching of the chitosan, and they can be overlapping in
337 the hybrids. Therefore, change in the N-H bending can be an indication of interaction
338 between HA/CS via hydrogen bonding. This result suggested weak interaction between
339 HA and CS.

340 FTIR spectra (Fig. 2i) for hybrids showed typical absorptions of HA, silylated
341 HA and CS as displayed in Table SM1. Typical band of C=O strectching of
342 glutaraldeyde at 1730 cm^{-1} was absent.

343

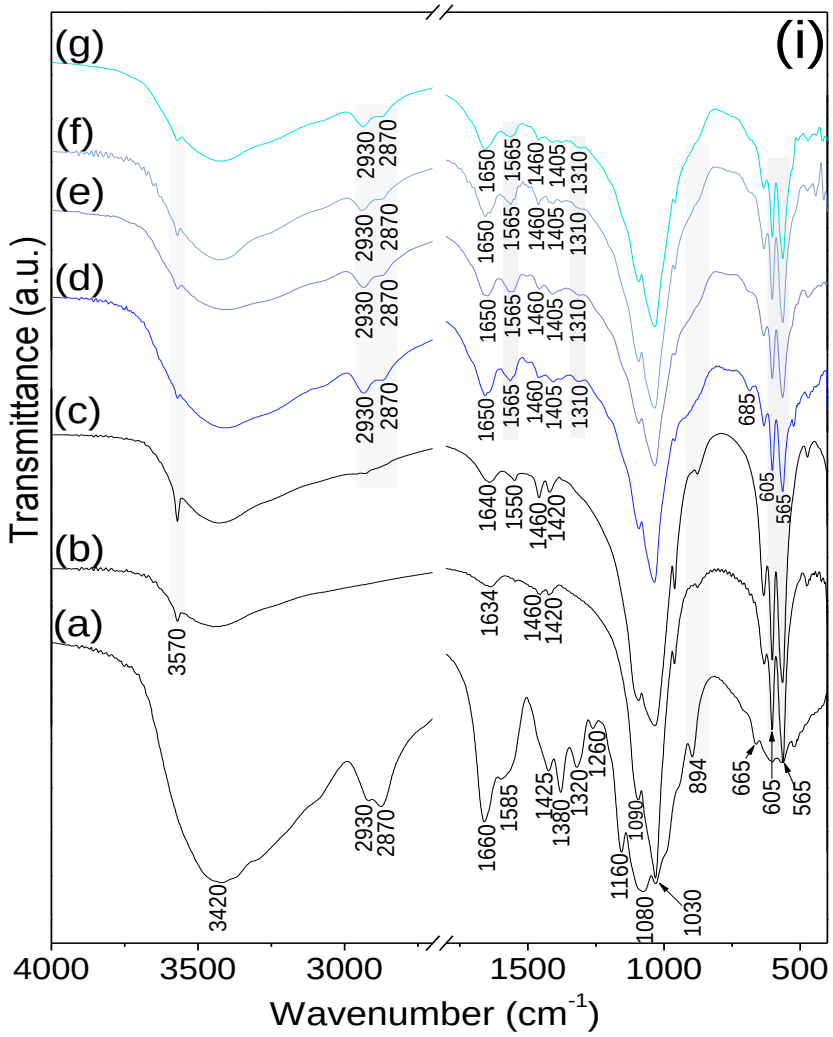

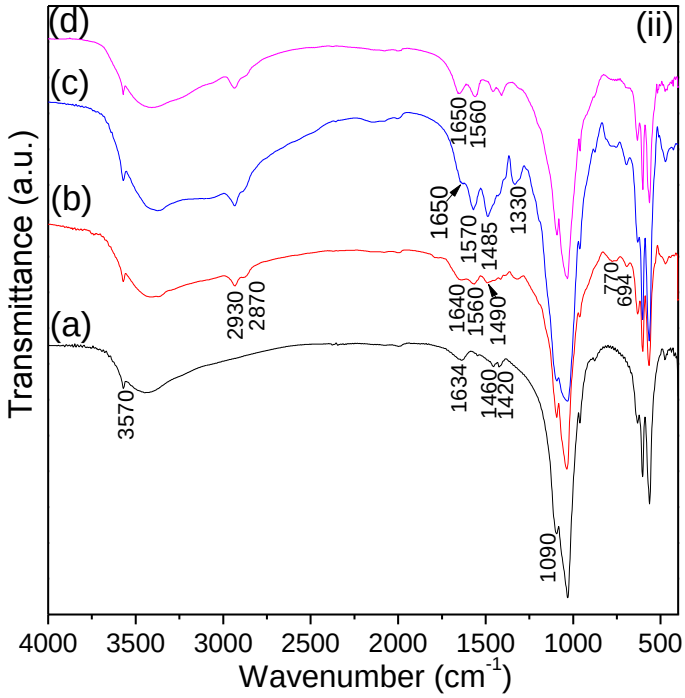

344

345

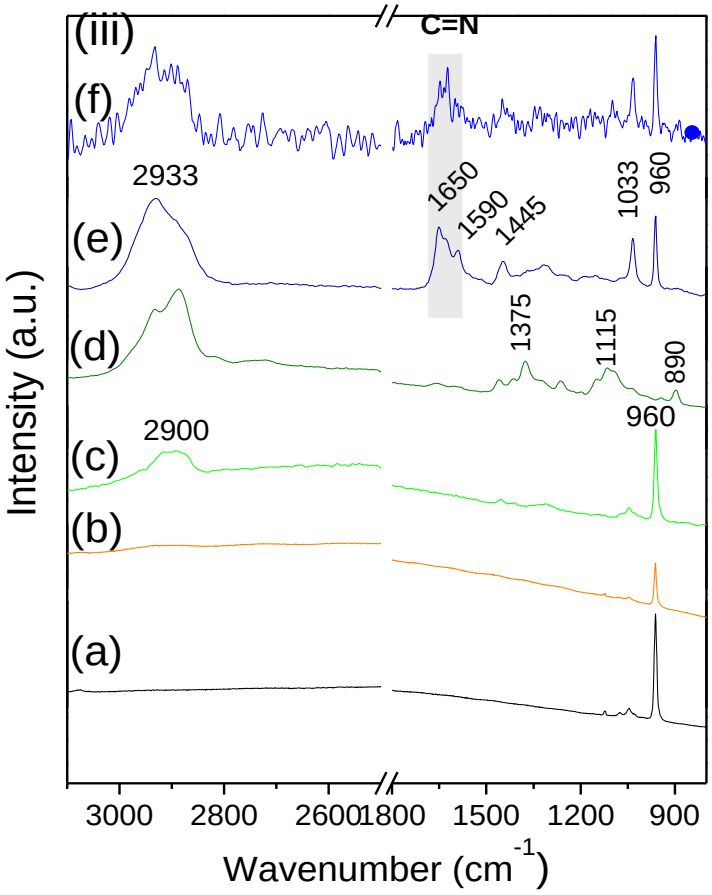

346

347

Figure 2. Infrared spectra of (i) (a) CS, (b) HA, (c) HA/CS, (d) HA-NH_2/CS-3, (e) HA-NH_2/CS-4, (f) HA-NH_2/CS-5 and (g) HA-NH_2/CS-6, (ii) (a) HA, (b) HA-NH_2, (c) HA-NH_2-GLU, (d) HA-NH_2-GLU-NaB and (iii) Raman spectra of (a) HA, (b) CS, (c) HA/CS (d) HA-NH_2, (e) HA-NH_2/CS-3, (f) HA-NH_2/CS-4, (g) HA-NH_2/CS-5 and (h) HA-NH_2/CS-6.

For hybrids the shift of the band from at 1655 cm^{-1} was associated to the presence of an interaction between HA-NH2 and CS. A possible mechanism of HA-NH_2 and CS crosslinking involves amino groups and formation of C=N bond between the amine groups of HA-NH_2 and CS and the carbonyl of Glu. For the hybrids (Fig. 2i), the band at 1655 cm^{-1} can be assigned to C=N stretching, suggesting the presence of an imine group (Atak et al., 2017; Ramachandran, Nandhakumar, & Dhanaraju, 2011). Other studies suggested that C=N stretching is located in the 1660 – 1630 cm^{-1} region (Frick, Ambrosi, Pollo, & Tessaro, 2018; Poon et al., 2014). However, this attribution is not definite considering that the band overlap with the C=O stretching and NH_2 deformation of CS at 1664 cm^{-1}. Similar results were obtained for chitosan crosslinker with Glu (Frick et al., 2018; Pratt, Wilson, & Kozinski, 2013). The band at 1560 cm^{-1} corresponds to C=C and/or NH bending (Liu, Thormann, Claesson, & Tyrode, 2014). Change in the NH_2 deformation initially at 1577 cm^{-1} in HA-NH_2 and CS, which shifted to 1560 cm^{-1} in the hybrids can also be associated to unreacted NH_3^+, offering adsorption sites for DS (Pratt et al., 2013; Shi et al., 2017).

Furthermore, in the HA-NH_2 sample, the bands associated to OH stretching and PO_4^{3-} didn't shift, suggesting that these latter groups of the HA-NH_2 did not interacted with CS.

The Raman spectrum of HA-NH_2 (Fig. 2ii) showed a band at 2900 cm^{-1} associated with CH_2 asymmetric stretching, suggesting the successful silylation of HA. The band at 960 cm^{-1} was assigned to P-O symmetric stretching of PO_4^{3-} (Lin -Vien et al., 1991).

The Raman spectrum of pure chitosan presented bands at 1375 cm^{-1} (CH_2 deformation), 1115 cm^{-1} C-N stretching in C-2 (Mahaninia & Wilson, 2017) and 890 cm^{-1}, C-C stretching of the pyranose monomers and C-O-C symmetric stretching of the ether groups (Lin-Vien et al., 1991).

For the hybrids, a CH_2 stretching was observed at 2933 cm^{-1}, possibly due to the presence of new groups. Furthermore, the presence of the Schiff base was confirmed by the new band at 1650 cm^{-1}, assigned to C=N stretching. Antisymmetric stretching was observed at C=C at 1590 cm^{-1} (Liu et al., 2014) and CH_2 deformation at 1445 cm^{-1}. For pure HA/CS spectrum, only absorptions of the HA were present and absence of the band at 1650 cm^{-1}, is a strong evidence of the absence of the C=N moieties.

3.1.3 ^{13}C NMR

^{13}C NMR spectrum of the organofunctionalized hydroxyapatite (Fig. 3a) exhibited three characteristic peaks at 11, 23 and 43 ppm, associated to carbons in the 3-aminopropyl, which confirmed the silylation of the HA (Goonasekera, Jack, Cooper-White, & Grøndahl, 2013). The peak at 164 ppm was attributed to carbonate (Pinto et al., 2011).

^{13}C NMR spectrum of the chitosan (Fig. 3f) presented peaks at 105, 83, 75 and 58 ppm assigned to C_1, C_4, $C_{3,5}$, $C_{2,6}$ of the polymer (Almeida et al., 2018; Rui et al., 2017). The peak at 169 ppm was assigned to C_7 (Monteiro & Airoldi, 1999) and 23 ppm is associated the incomplete deacetylation of the chitin (Almeida et al., 2018).

For the hybrids, ^{13}C NMR spectra (Fig. 3a-d) showed peaks of both silylated HA and CS and broader signal at 170-180 ppm, which can be associated to overlapping of the the signal of carbon in C=N and C=O , in concordance with Raman and infrared spectroscopies and also previous studies about reticulated chitosan (Monteiro & Airoldi, 1999; Ziegler-Borowska, Chełminiak, Kaczmarek, & Kaczmarek-Kędziera, 2016). However, ^{13}C NMR spectra presented new two signals at 128 and 143 ppm and were assigned to C=C (Monteiro & Airoldi, 1999). The latter group indicated the tautomeric species of the imine groups in acid medium (Nick, Stuart, Jonathan, Nick, & Stuart, 2012).

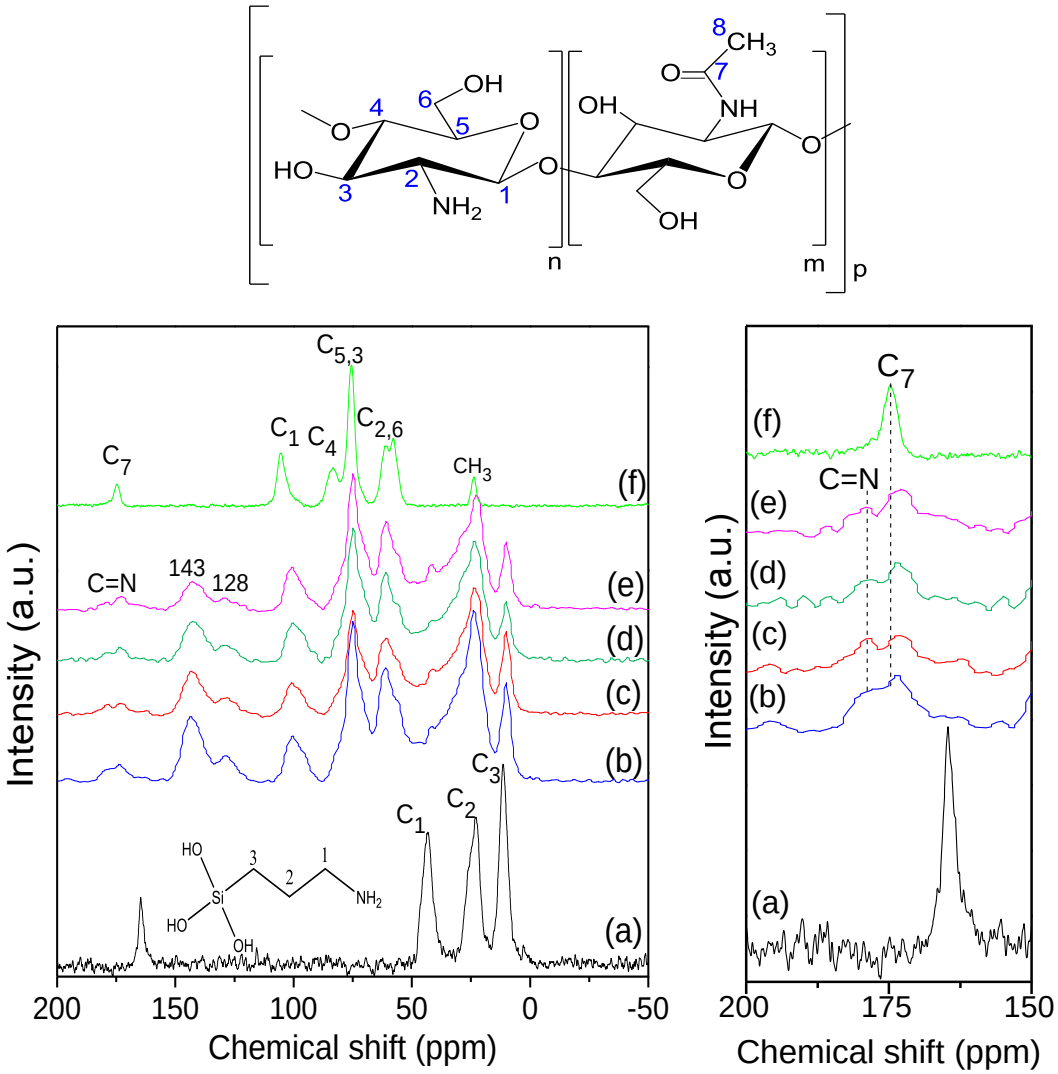

Figure 3. ^{13}C NMR spectra of (a) HA-NH_2, (b) HA-NH_2/CS-3, (c) HA-NH_2/CS-4, (d) HA-NH_2/CS-5 (e) HA-NH_2/CS-6 and (f) CS. *signal at 165 ppm is assigned to carbonate impurity in the pristine HA.

3.1.4 CHN elemental analysis and mechanism of crosslinking

The quantification of the organic groups in the hybrids was based on CHN elemental analysis (Table 1). For pristine HA, a low content of carbon was detected, possibly due the presence of carbonate. The quantity of nitrogen in HA-NH_2 indicated the presence of 1.80 mmol g^{-1} organic anchored moieties on the HA surface.

Table 1. CHN elemental analysis of HA-NH_2, CS and their bionanohybrids obtained by *crosslinking* with Glu and the specific surface area results (SA) for the hybrids.

Sample	%C	%H	%N	Q_C (mmol g^{-1})	Q_N (mmol g^{-1})	C/N	SA (m2 g^{-1})
HA-NH_2	6.50	1.90	2.50	5.41	1.80	3.03	13
HA-NH_2/CS-3	22.63	3.94	2.55	18.86	1.82	10.35	24
HA-NH_2/CS-4	21.46	3.76	2.10	17.88	1.49	11.92	34
HA-NH_2/CS-5	18.20	3.19	1.78	15.15	1.27	11.93	45
HA-NH_2/CS-6	19.56	3.50	2.11	16.56	1.50	11.04	50

*Q is the amount of carbon (C) or nitrogen (N).

For pure chitosan, high CHN contents were observed, and the data were consistent with the chitosan composition. For all composites, high organic contents were observed, and the CHN quantities increased for reactions at lower pH compared to reactions at higher pH. Small differences (~1.2-1.4%) were observed between pH 3 and 4 and pH 5 and 6. Considering the nitrogen percentages, the quantity of amino groups was greater for HA-NH_2/CS-3 and HA-NH_2/CS-4 than for the other samples.

Similar behavior was observed for the crosslinking of chitosan with Glu (Lal, Arora and Sharma 2016). The lower C/N mol ratio observed for HA-NH_2/CS-3 can be related to the presence of unreacted and protonated amino groups. This behavior suggests that the formation of the imine at pH 3.0 is not effective because of the protonation of the NH_2 groups in more acidic medium and the consequently lower probability of C=N formation. On the other hand, more favorable conditions for the formation of the Schiff base occurred at pH 4 to 5 due the presence of unprotonated NH_2 groups and protonated carbonyl groups, which are reactive species in the formation of C=N bonds (Antony et al., 2019; Kildeeva, Perminov, Vladimirov, Novikov, & Mikhailov, 2009).

Based on specific surface area results and the amount of nitrogen in the solids (Table 1), different density of amino groups were observed: for example, for HA-NH_2/CS-3 and HA-NH_2/CS-4, the values were 0.076 and 0.044 mmol of N per m^2, while 0.03 of N per m^2 for other two hybrids. This aspect can influence the performance of the solids during the drug adsorption.

These results are in accordance with the vibrational spectroscopy and ^{13}C NMR results and suggest the occurrence of bonding among HA-NH_2, Glu, and CS. Based on the characterization results, the mechanism of crosslinking (Figure SM2) and the structure of the hybrids are proposed in Figure 4. The proposed mechanism considers that Glu species at acid pH are the monomeric molecule (Kildeeva et al., 2009; Migneault, Dartiguenave, Bertrand, & Waldron, 2004).

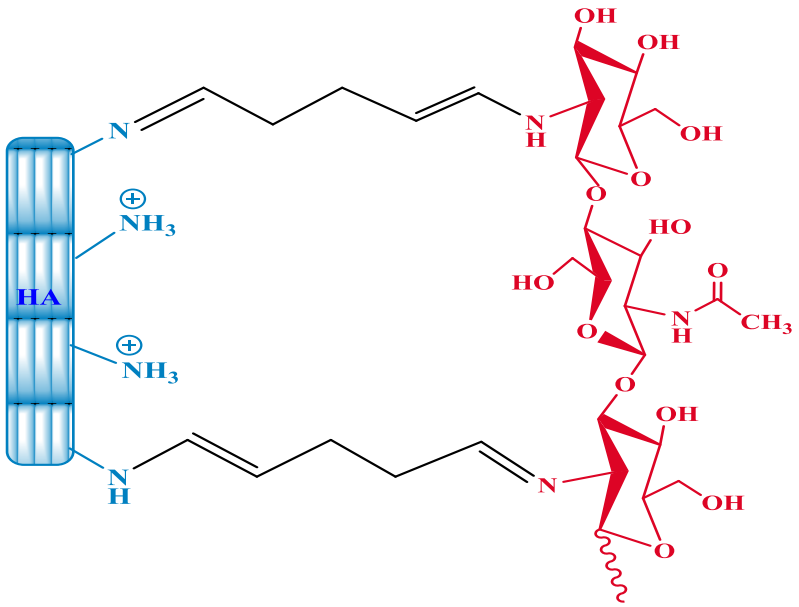

Figure 4. Structure of the amino-hydroxyapatite reticulated glutaraldehyde chitosan hybrids. Impurity of carbonate in apatite was not considered.

3.1.6 Thermal analysis

Thermogravimetric curves (TG/DTG) of hydroxyapatite, chitosan and their hybrids are shown in Figure SM3. The thermal degradation of the silanized hydroxyapatite presented three stages of 3.9%, 12.2% and 0.8% mass loss, which were attributed to the loss of water adsorbed at 25-185 °C, decomposition of the silane covalently bonded to the inorganic matrix in the range of 185 to 635 °C (Lung et al. 2016; Silva et al. 2006), and hydroxyapatite decomposition, respectively (Costa et al. 2009; Adolfsson et al. 2004; Locardi et al. 1993).

$$Ca_{10}(PO_4)_6(OH)_2 \rightarrow Ca_{10}(PO_4)_6(OH)_{2-2x}O + xH_2O$$

492

493 Pristine chitosan showed a 7% initial mass loss, which was associated with the
494 loss of adsorbed water (Lal et al., 2016). Subsequent events showed 38 and 13.4%
495 thermal degradation and were attributed to the degradation of the biopolymer by
496 depolymerization of the chains and decomposition of the pyranose rings followed by
497 dehydration, deamination and finally ring-opening reactions (Wanjun et al., 2015,
498 Zawadzki and Kaczmarek, 2010).

499 Hybrids presented similar thermal degradation profilesinfluenced by the pH
500 during the synthesis. All thermogravimetric assignments are listed in Table SM2.

501 Three mass loss events are identified in all hybrids. The first one (20 - 131 °C)
502 was associated with the elimination of the adsorbed water (Ruphuy et al., 2016). The
503 second in the 131 - 354º C range and third stages at 346 - 642 ºC corresponded to the
504 thermal decomposition of the organic part of the hybrids. In addition, the third event
505 occurred in the temperature range for the crosslinking reaction with glutaraldehyde
506 (Mohamed and Wilson, 2016). A similar result was described for HA/CS hybrids
507 obtained with 17 and 23% weight/weight chitosan (Zima et al., 2018).

508 The residual percentages were 54.8%, 61.4%, 67.2% and 63,9% for the HA-
509 NH_2/CS-3, HA-NH_2/CS-4, HA-NH_2/CS-5 and HA-NH_2/CS-6 solids, respectively, and
510 were associated with the inorganic part of the hybrids.

511 The order of thermal stability was HA.NH_2/CS-5 > HA.NH_2/CS-6 >
512 HA.NH_2/CS-4 > HA.NH_2/CS-3. Therefore, the system obtained at pH 3 presented lower
513 thermal stability than the other hybrids, which was associated with pH 3 disfavoring
514 formation of the imine, as indicated by the CHN analysis and other studies in the
515 literature, since crosslinking results in thermally stable structures (Antony et al., 2019;

Baldino, Concilio, Cardea, De Marco, & Reverchon, 2015). However, the thermal stability of the HA-NH_2/CS-3 solid was better than that of pristine chitosan.

Based on TG results, the hybrids with higher organic contents were the ones prepared at pH 3 and 4, and were in concordance with CHN results. This result indicated that unreacted NH_2 groups are free for drug interaction.

3.1.5 Scanning electron microscopy

All nanocomposites presented a uniform surface without polymeric or inorganic aggregates, indicating the homogeneous dispersion of each component in the hybrids and particles with irregular shapes and rough surface (Fig. SM4).

3.2 Adsorption of diclofenac sodium

3.2.1 Influence of the composition and Zeta potential measurements

The influence of pH on drug adsorption was investigated at pH 6 -12 for all hybrids (Fig. SM5i). For pH below 6, precipitation of the drug was detected. Better drug adsorptions were obtained at lower investigated pH, following the Zeta potential results. Zeta potential measurements (Fig. SM5ii) suggested that increasing the pH during synthesis influenced the isoelectric point, which was 9.3, 8.5, 7.1 and 6.55 for the hybrids obtained at pH 3, 4, 5 and 6, respectively. At pH values higher than the zeta potential, the surfaces of the hybrids are negatively charged, which would tend to cause electrostatic repulsion between the hybrids and DS. Therefore, pH 6 was selected for adsorption studies.

A positive and higher Zeta potential was obtained for HA-NH_2/CS-3 in relation to the other hybrids. Considering that the pH in the removal test was 6, both HA-

NH_2/CS-3 and HA-NH_2/CS-4 are positively charged at this pH, and therefore, both surfaces are favorable for DS removal, as its pKa is 4.1 (De Oliveira et al., 2017; Hiew et al., 2019). Thus, a better interaction with the anionic drug was established by the hybrids with greater cationic character—in this case, HA-NH_2/CS-3.

The zeta potential measurements for HA-NH_2/CS-3 were not possible below pH 4 because the system was not stabilized. This finding is an indication that the population of imine and unreacted amino groups is dependent on the experimental conditions used to obtain the hybrids at different pH (Kamari, Ngah, Chong, & Cheah, 2009; M. G. Li, Cheng, & Yan, 2007).

Accordingly, (See Fig. SM5i and Table SM3), HA-NH_2/CS-3 hybrid presented a high drug removal capacity of 45 mg g^{-1} (95%), while for the HA-NH_2/CS-6 hybrid, the value was 35 mg g^{-1} (77%). All values detected for the composites were higher than those detected for pure (3.4 mg g^{-1}) and silylated HA (11.9 mg g^{-1}) and CS (22.4 mg g^{-1}). The results can be related to the surface charge of the various hybrids, as when the crosslinking reaction is conducted in an acidic medium, not only increased imine formation but also protonation of the unreacted amino groups occurs.

3.2.2 Influence of the adsorbent dose

Test investigating the influence of the adsorbent dose were performed on the composites with higher removal efficiencies, namely, HA-NH_2/CS-3 and HA-NH_2/CS-4 (Fig. SM6). The results indicated an increase in the amount of drug removed until an equilibrium was reached above 50 mg of the hybrid, and 95% removal (50.5 mg g^{-1}) was achieved by HA-NH_2/CS-3.

567 HA-NH_2/CS-4 did not show a variation in drug removal efficiency, and the
568 values were approximately the same (91%) for adsorbent doses between 25 and 100 mg.
569
570 *3.2.3 Kinetic study*
571
572 The effect of time on drug removal (Fig. SM7) indicated that an equilibrium was
573 reached at 30 and 15 min and that the maximum removal was 52 mg and 45 mg g^{-1} for
574 HA-NH_2/CS-3 and HA-NH_2/CS-4, respectively.
575 Different equilibrium times were observed for DS adsorption on different studies
576 on the literature. For example, Feng et al. (2018) obtained 10 mg L^{-1} DS removal with
577 graphene-chitosan composites in 1 h. Soares, Fernandes, Sacramento, Trindade, &
578 Daniel-da-silva, (2019) observed 100 mg L^{-1} DS removal with magnetite coated with
579 chitosan in 5 h at pH 6.
580 Results of the data were fitted kinetic models are presented in Table 2. Both
581 systems were well fitted with a second-order kinetic model, as indicated by the
582 correlation coefficient and small difference between the theoretical and experimental
583 adsorption capacities.
584 **Table 2.** Kinetic and equilibrium parameters obtained from nonlinear fitting of the data
585 with the pseudo-first-order, pseudo-second-order and Elovich equations for the
586 adsorption of DS on HA-NH_2/CS-3 and HA-NH_2/CS-4 at 25 °C, pH 6 and 100 mg L^{-1}
587 and according to the nonlinear Langmuir model.

Models	Sample	
	Kinetic models	
	HA-NH_2/CS-3	HA-NH_2/CS-4

$q_{e(exp)}$ (mg g^{-1})	51.9	45.2
Pseudo-first-order		
$q_{e(teor.)}$ (mg g^{-1})	50.5±0.7	45.2±0.1
K_1 (g min^{-1})	1.0±0.2	1.4±0.1
R^2	0.9756	0.9991
SD (mg g^{-1})	2.3	0.4
Pseudo-second-order		
$q_{e(teor.)}$ (mg g^{-1})	51.9±0.5	45.5±0.1
k_2 (10^{-2} g mg^{-1} min^{-1})	4.182±0.67	0.139±0.01
R^2	0.9931	0.9999
SD (mg g^{-1})	1.2	0.1
Elovich		
α (mg g^{-1} min^{-1})	(16.10±6.10) 10^9	(2.07±36.0) 10^{33}
β (g mg^{-1})	0.5±0.1	1.8±0.4
R^2	0.9919	0.9981
SD (mg g^{-1})	1.3	0.5
Equilibrium model		
Langmuir		
$q_{e\ (exp)}$ (mg g^{-1})	125.0	65.7
$q_{máx}$ (mg g^{-1})	139.5 ± 4.0	74.1 ± 1.0
K_L (10^{-2} L mg^{-1})	4.8 ± 0.4	4.2 ± 0.2
R^2	0.9899	0.9976
SD	4.72	1.24

588 *3.2.4 Influence of initial DS concentration*

589

590 The influence of the initial DS concentration was evaluated in the range of 1 –
591 500 mg L^{-1} in the equilibrium time and pH 6 (Fig. 5). The adsorption was more
592 pronounced at the lower DS concentrations than at the higher DS concentration until an
593 equilibrium was reached at 140 mg L^{-1}, showing a maximum adsorption of 125 mg of
594 adsorbed DS per gram of HA-NH_2/CS-3. The same behavior was observed for HA-
595 NH_2/CS-4 with a maximum adsorption of 65.7 mg g^{-1}, which was half of the value

observed for HA-NH_2/CS-3. This behavior can be associated with the lower quantity of organic moieties on HA-NH_2/CS-4 than on HA-NH_2/CS-3, as indicated by the CHN data.

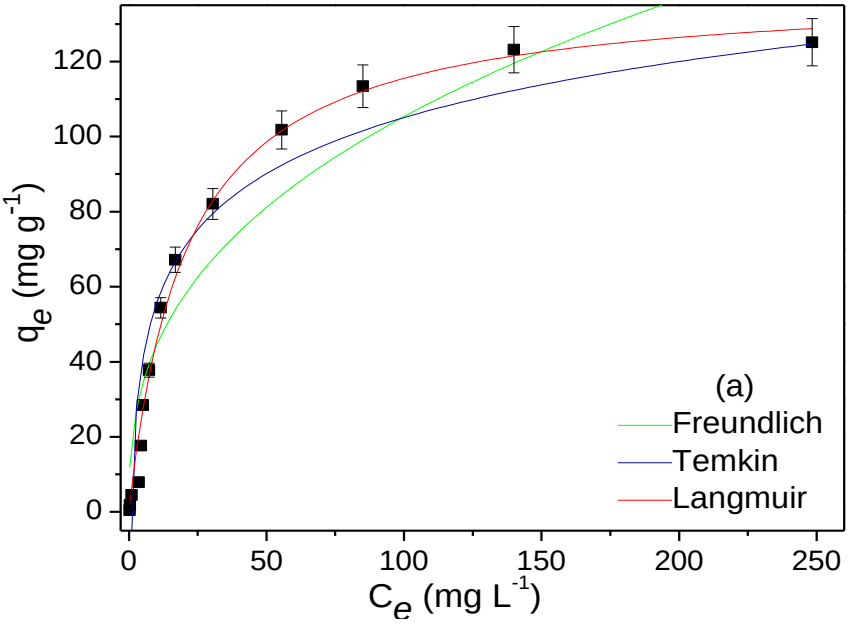

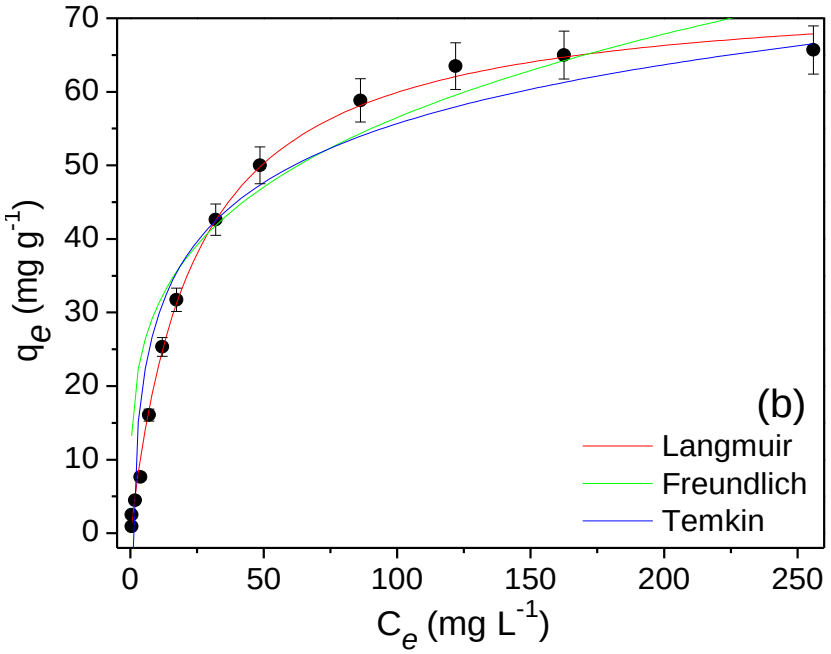

606 **Figure 7.** Isotherms and their nonlinear fitting with equilibrium models for DS
607 adsorption by (a) HA-NH_2/CS-3 and (b) HA-NH_2/CS-4.
608
609 The removal data were fitted with Langmuir model, as summarized in Table 2.
610
611 Both systems were well fitted by the Langmuir model, showing a correlation
612 coefficients greater than 0.98, although the SD between the experimental and theoretical
613 maximum q was lower for HA-NH_2/CS-4 than for HA-NH_2/CS-3.
614 Compared with those from other studies, these adsorption results were promising
615 (Table SM4). The synthesized hybrids presented higher adsorption capacities than other
616 modified chitosan materials. Furthermore, lower adsorption for the precursors, HA-NH_2
617 (11.91 mg g^{-1}) and CS (22.43 mg g^{-1}), illustrates the synergism between the
618 constituents in the hybrids and improvement of the drug adsorption.
619
620 *3.2.5 Mechanism of the interaction of drug/* hybrid
621 Infrared spectra of the hybrids after drug removal (Fig. SM6) indicated new
622 bands associated with drug were observed at 1310, 1581 and 1507 cm^{-1}, assigned to
623 C=O and C=C stretching (Kaur & Datta, 2014; Kumar et al., 2018).
624 The mechanism of the interaction between DS and the hybrids was suggested
625 based on the characteristics of the modified surface and the drug in solution. At pH 6.0,
626 the anionic form of the DS molecule (deprotonated species) is predominant, considering
627 that its pKa is 4.1 (Hu et al., 2019; Lessa et al., 2018; Lonappan et al., 2017).
628 As indicated by the zeta potential, the surfaces are positively charged at pH 6;
629 therefore, electrostatic interactions between the charged species can be the principal
630 mechanism of interaction (Fig. SM7). The same behavior was proposed for chitosan

631 reticulated with Glu (Riegger et al. 2018) and for CS reticulated with genipin
632 (Lonappan et al., 2018). Other mechanisms acting in synergy with electrostatic
633 interactions and promoting the adsorption efficiency can be present, i.e., hydrogen
634 bonding through the free polar groups -OH and -NH_2 and van der Waals forces (Liang
635 et al., 2019; Soares et al., 2019). In addition, the crosslinking of chitosan also breaks the
636 hydrogen bonds between adjacent units of the polymer, which may result in partial
637 breaking of the chitosan structure and the release of additional free polar groups (OH),
638 thereby promoting the removal of DS via the hydroxyl sites of chitosan (Wilson & Xue,
639 2013).
640
641
642 **4. Conclusion**
643
644 Silylated HA/Glu/CS hybrids were synthesized at pH 3, 4, 5 and 6. Control
645 reaction of amino hydroxyapatite and glutaraldehyde following by reduction indicated
646 that C=N formation is the main mechanism of interaction between amino modified HA
647 and aldehyde. The XRD, FTIR, Raman, ^{13}C NMR and CHN analysis results confirmed
648 the formation of hybrid possibly by interaction between the amine groups present in HA
649 and chitosan and the aldehyde groups present in the bifunctional agent, resulting in a
650 new inorganic-organic hybrid. The difference between all hybrids relies on the amount
651 of organic parts as indicated in CHN analysis and thermogravimetry.
652 The hybrid HA-NH_2/CS-3 presented higher cationic character than the hybrid
653 HA-NH_2/CS-4, and the difference in surface charge was likely responsible for the
654 different adsorptive properties of the materials for DS. HA-NH_2/CS-3 presented better
655 drug adsorption performance than HA-NH_2/CS-4 at pH 6 and the maximum removal
656 capacity obtained was 125 and 65.7 mg g^{-1}, respectively.

This work demonstrates that HA/chitosan hybrids were obtained and functioned as promising biosorbents for the remediation of effluents contaminated with DS.

Acknowledgments

To National Council for Scientific and Technological Development (CNPq, Brazil) for financial support, M.G. Fonseca (Grant 310921/2017-1) and M.B.B. Pereira (Grant 164614/2014-1). The authors are also thankful to Prof D.L.A. Faria (IQ-USP) for the Raman spectra.

References

Acuña, V., Ginebreda, A., Mor, J. R., Petrovic, M., Sabater, S., Sumpter, J., & Barceló, D. (2015). Balancing the health bene fi ts and environmental risks of pharmaceuticals : Diclofenac as an example. *Environment International*, *85*, 327–333. https://doi.org/10.1016/j.envint.2015.09.023

Adolfsson, E., Nygren, M., & Hermansson, L. (2004). Decomposition Mechanisms in Aluminum Oxide-Apatite Systems. *Journal of the American Ceramic Society*, *82*(10), 2909–2912. https://doi.org/10.1111/j.1151-2916.1999.tb02176.x

Almeida, R. R., Damasceno, E. T. S., de Carvalho, S. Y. B., de Carvalho, G. S. G., Gontijo, L. A. P., & Guimarães, L. G. de L. (2018). Chitosan nanogels condensed to ferulic acid for the essential oil of Lippia origanoides Kunth encapsulation. *Carbohydrate Polymers*, *188*, 268–275. https://doi.org/10.1016/j.carbpol.2018.01.103

Antony, R., Arun, T., & Manickam, S. T. D. (2019). A review on applications of chitosan-based Schiff bases. *International Journal of Biological Macromolecules*, *129*, 615–633. https://doi.org/10.1016/j.ijbiomac.2019.02.047

Atak, B. H., Buyuk, B., Huysal, M., Isik, S., Senel, M., Metzger, W., … Cetin, G. (2017). Preparation and characterization of amine functional nano-hydroxyapatite/chitosan bionanocomposite for bone tissue engineering applications. *Carbohydrate Polymers*, *164*, 200–213.

https://doi.org/10.1016/j.carbpol.2017.01.100
Baldino, L., Concilio, S., Cardea, S., De Marco, I., & Reverchon, E. (2015). Complete glutaraldehyde elimination during chitosan hydrogel drying by SC-CO2 processing. *Journal of Supercritical Fluids*, *103*, 70–76. https://doi.org/10.1016/j.supflu.2015.04.020
Basheer, A. A. (2018). New generation nano-adsorbents for the removal of emerging contaminants in water. *Journal of Molecular Liquids*, *261*, 583–593. https://doi.org/10.1016/J.MOLLIQ.2018.04.021
Bayrak, G. K., Demirtaş, T. T., & Gümüşderelioğl, M. (2017). Microwave-induced biomimetic approach for hydroxyapatite coatings of chitosan scaffolds. *Carbohydrate Polymers*, *157*, 803–813. https://doi.org/10.1016/j.carbpol.2016.10.016
Bonnefille, B., Gomez, E., Courant, F., Escande, A., & Fenet, H. (2018). Diclofenac in the marine environment: A review of its occurrence and effects. *Marine Pollution Bulletin*, *131*, 496–506. https://doi.org/10.1016/j.marpolbul.2018.04.053
Chatterjee, S., Gupta, A., Mohanta, T., Mitra, R., Samanta, D., Mandal, A. B., … Singha, N. R. (2018). Scalable Synthesis of Hide Substance-Chitosan-Hydroxyapatite: Novel Biocomposite from Industrial Wastes and Its Efficiency in Dye Removal. *ACS Omega*, *3*(9), 11486–11496. research-article. https://doi.org/10.1021/acsomega.8b00650
Ciaccia, M., & Di Stefano, S. (2015). Mechanisms of imine exchange reactions in organic solvents. *Organic & Biomolecular Chemistry*, *13*(3), 646–654. https://doi.org/10.1039/C4OB02110J
De Oliveira, T., Guégan, R., Thiebault, T., Milbeau, C. Le, Muller, F., Teixeira, V., … Boussafir, M. (2017). Adsorption of diclofenac onto organoclays: Effects of surfactant and environmental (pH and temperature) conditions. *Journal of Hazardous Materials*, *323*, 558–566. https://doi.org/10.1016/J.JHAZMAT.2016.05.001
Deepthi, S., Venkatesan, J., Kim, S. K., Bumgardner, J. D., & Jayakumar, R. (2016). An overview of chitin or chitosan/nano ceramic composite scaffolds for bone tissue engineering. *International Journal of Biological Macromolecules*, *93*, 1338–1353. https://doi.org/10.1016/j.ijbiomac.2016.03.041
Dorozhkin, S. V. (2012). Dissolution mechanism of calcium apatites in acids: A review of literature. *World Journal of Methodology*, *2*(1), 1.

https://doi.org/10.5662/wjm.v2.i1.1
Elliott J.C. (1994). Structure and Chemistry of the Apatites and other Calcium Orthophosphates. *Elsevier, Amsterdam*, 404.
Feng, Z., Odelius, K., & Hakkarainen, M. (2018). Tunable chitosan hydrogels for adsorption: Property control by biobased modifiers. *Carbohydrate Polymers*, *196*, 135–145. https://doi.org/10.1016/j.carbpol.2018.05.029
Fonseca, M. G. d., & Airoldi, C. (1999). Action of silylating agents on a chrysotile surface and subsequent reactions with 2-pyridine and 2-thiophene carbaldehydes. *Journal of Materials Chemistry*, *9*(6), 1375–1380. https://doi.org/10.1039/a807383j
Frick, J. M., Ambrosi, A., Pollo, L. D., & Tessaro, I. C. (2018). Influence of Glutaraldehyde Crosslinking and Alkaline Post-treatment on the Properties of Chitosan-Based Films. *Journal of Polymers and the Environment*, *26*(7), 2748–2757. https://doi.org/10.1007/s10924-017-1166-3
Goonasekera, C. S., Jack, K. S., Cooper-White, J. J., & Grøndahl, L. (2013). Attachment of poly(acrylic acid) to 3-aminopropyltriethoxysilane surface-modified hydroxyapatite. *Journal of Materials Chemistry B*, *1*(42), 5842–5852. https://doi.org/10.1039/c3tb21110j
Harja, M., & Ciobanu, G. (2018). Studies on adsorption of oxytetracycline from aqueous solutions onto hydroxyapatite. *Science of the Total Environment*, *628–629*, 36–43. https://doi.org/10.1016/j.scitotenv.2018.02.027
Hassan, A. F., & Hrdina, R. (2018). Chitosan/nanohydroxyapatite composite based scallop shells as an efficient adsorbent for mercuric ions: Static and dynamic adsorption studies. *International Journal of Biological Macromolecules*, *109*, 507–516. https://doi.org/10.1016/J.IJBIOMAC.2017.12.094
Hiew, B. Y. Z., Lee, L. Y., Lai, K. C., Gan, S., Suchithra, T., & Pan, G.-T. (2019). Adsorptive decontamination of diclofenac by three-dimensional graphene-based adsorbent: Response surface methodology, adsorption equilibrium, kinetic and thermodynamic studies. *Environmental Research*, *168*, 241–253. https://doi.org/10.1016/j.envres.2018.09.030
Hu, D., huang, H., Jiang, R., Wang, N., Xu, H., Wang, Y.-G., & Ouyang, X. (2019). Adsorption of diclofenac sodium on bilayer amino-functionalized cellulose nanocrystals/chitosan composite. *Journal of Hazardous Materials*, *369*, 483–493. https://doi.org/10.1016/j.jhazmat.2019.02.057

Huang, Z., Yu, B., Feng, Q., Li, S., Chen, Y., & Luo, L. (2011). In situ-forming chitosan/nano-hydroxyapatite/collagen gel for the delivery of bone marrow mesenchymal stem cells. *Carbohydrate Polymers*, *85*(1), 261–267. https://doi.org/10.1016/j.carbpol.2011.02.029

Jó, T., Filipkowska, U., Szymczyk, P., Rodziewicz, J., Mielcarek, A., Jóźwiak, T., … Mielcarek, A. (2017). Effect of ionic and covalent crosslinking agents on properties of chitosan beads and sorption effectiveness of Reactive Black 5 dye. *Reactive and Functional Polymers*, *114*, 58–74. https://doi.org/10.1016/j.reactfunctpolym.2017.03.007

Kamari, A., Ngah, W. S. W., Chong, M. Y., & Cheah, M. L. (2009). Sorption of acid dyes onto GLA and H 2 SO 4 cross-linked chitosan beads. *DES*, *249*(3), 1180–1189. https://doi.org/10.1016/j.desal.2009.04.010

Kaur, M., & Datta, M. (2014). Diclofenac Sodium Adsorption onto Montmorillonite: Adsorption Equilibrium Studies and Drug Release Kinetics. *Adsorption Science & Technology*, *32*(5), 365–387. https://doi.org/10.1260/0263-6174.32.5.365

Kildeeva, N. R., Perminov, P. A., Vladimirov, L. V, Novikov, V. V, & Mikhailov, S. N. (2009). About Mechanism of Chitosan Cross-Linking with Glutaraldehyde. *Russian Journal of Bioorganic*, *35*(3), 360–369. https://doi.org/10.1134/S106816200903011X

Kumar, S., Sharma, R. P., Venugopalan, P., Ferretti, V., Perontsis, S., & Psomas, G. (2018). Copper(II) diclofenac complexes: Synthesis, structural studies and interaction with albumins and calf-thymus DNA. *Journal of Inorganic Biochemistry*, *187*, 97–108. https://doi.org/10.1016/J.JINORGBIO.2018.07.009

Kyzas, G. Z., Bikiaris, D. N., & Lazaridis, N. K. (2008). Low-Swelling Chitosan Derivatives as Biosorbents for Basic Dyes. *Langmuir*, *24*(7), 4791–4799. https://doi.org/10.1021/la7039064

Lal, S., Arora, S., & Sharma, C. (2016). Synthesis , thermal and antimicrobial studies of some Schiff bases of chitosan. *Journal of Thermal Analysis and Calorimetry*, *124*(2), 909–916. https://doi.org/10.1007/s10973-015-5227-3

Leceta, I., Guerrero, P., Cabezudo, S., & De La Caba, K. (2013). Environmental assessment of chitosan-based films. *Journal of Cleaner Production*, *41*, 312–318. https://doi.org/10.1016/j.jclepro.2012.09.049

Lessa, E. F., Nunes, M. L., & Fajardo, A. R. (2018). Chitosan/waste coffee-grounds composite: An efficient and eco-friendly adsorbent for removal of pharmaceutical

790 contaminants from water. *Carbohydrate Polymers*, *189*, 257–266.
791 https://doi.org/10.1016/j.carbpol.2018.02.018
792 Li, M. G., Cheng, S., & Yan, H. (2007). Preparation of crosslinked chitosan/poly(vinyl
793 alcohol) blend beads with high mechanical strength. *Green Chemistry*, *9*(8), 894.
794 https://doi.org/10.1039/b618045k
795 Li, Y., Liu, T., Zheng, J., & Xu, X. (2013). Glutaraldehyde-Crosslinked Chitosan /
796 Hydroxyapatite Bone Repair Scaffold and Its Application as Drug Carrier for
797 Icariin. *Journal of Applied Polymer Science*, 1539–1547.
798 https://doi.org/10.1002/app.39339
799 Liang, X. X., Omer, A. M. M., Hu, Z. hong, Wang, Y. guang, Yu, D., & Ouyang, X.
800 kun. (2019). Efficient adsorption of diclofenac sodium from aqueous solutions
801 using magnetic amine-functionalized chitosan. *Chemosphere*, *217*, 270–278.
802 https://doi.org/10.1016/j.chemosphere.2018.11.023
803 Lin-Vien, D., Colthup, N., Fateley, W., & Grasselli, J. (1991). The Handbook of
804 infrared and raman characteristic frequencies of organic molecules. *Academic*
805 *Press*, 15–503.
806 Liu, C., Thormann, E., Claesson, P. M., & Tyrode, E. (2014). Surface grafted chitosan
807 gels. Part II. Gel formation and characterization. *Langmuir*, *30*(29), 8878–8888.
808 https://doi.org/10.1021/la501319r
809 Locardi, B., Pazzaglia, U. E., Gabbi, C., & Profilo, B. (1993). Thermal behaviour of
810 hydroxyapatite intended for medical applications. *Biomaterials*, *14*(6), 437–441.
811 https://doi.org/10.1016/0142-9612(93)90146-S
812 Lonappan, L., Liu, Y., Rouissi, T., Pourcel, F., Brar, S. K., Vermaa, M., & Surampalli,
813 R. Y. (2018). Covalent immobilization of laccase on citric acid functionalized
814 micro-biochars derived from different feedstock and removal of diclofenac.
815 *Chemical Engineering Journal*, *351*, 985–994.
816 https://doi.org/10.1016/j.cej.2018.06.157
817 Lonappan, L., Rouissi, T., Kaur, S., Verma, M., & Surampalli, R. Y. (2017). An insight
818 into the adsorption of diclofenac on different biochars: Mechanisms, surface
819 chemistry and thermodynamics. *Bioresource Technology*, *249*, 386–394.
820 https://doi.org/10.1016/j.biortech.2017.10.039
821 Lu, F., & Astruc, D. (2018). Nanomaterials for removal of toxic elements from water.
822 *Coordination Chemistry Reviews*, *356*, 147–164.
823 https://doi.org/10.1016/j.ccr.2017.11.003

824 Luna, D. M. G., Budianta, W., Katrina, K., Rivera, P., & Arazo, R. O. (2017). Journal
825 of Environmental Chemical Engineering Removal of sodium diclofenac from
826 aqueous solution by adsorbents derived from cocoa pod husks. *Biochemical*
827 *Pharmacology*, *5*(2), 1465–1474. https://doi.org/10.1016/j.jece.2017.02.018
828 Mahaninia, M. H., & Wilson, L. D. (2017). Phosphate uptake studies of cross-linked
829 chitosan bead materials. *Journal of Colloid and Interface Science*, *485*, 201–212.
830 https://doi.org/10.1016/j.jcis.2016.09.031
831 Manatunga, D. C., De Silva, R. M., De Silva, K. M. N., & Ratnaweera, R. (2016).
832 Natural polysaccharides leading to super adsorbent hydroxyapatite nanoparticles
833 for the removal of heavy metals and dyes from aqueous solutions. *RSC Advances*,
834 *6*(107), 105618–105630. https://doi.org/10.1039/c6ra22662k
835 Migneault, I., Dartiguenave, C., Bertrand, M. J., & Waldron, K. C. (2004).
836 Glutaraldehyde: Behavior in aqueous solution, reaction with proteins, and
837 application to enzyme crosslinking. *BioTechniques*, *37*(5), 790–802.
838 https://doi.org/10.2144 / 04375rv01
839 Modrzejewska, Z., Skwarczyńska, A., Douglas, T. E. L., Biniaś, D., Maniukiewicz, W.,
840 & Sielski, J. (2015). Structure of chitosan gels mineralized by sorption. *Journal of*
841 *Molecular Structure*, *1098*, 101–109.
842 https://doi.org/10.1016/j.molstruc.2015.06.001
843 Monteiro, O. A. C. J., & Airoldi, C. (1999). Some studies of crosslinking chitosan –
844 glutaraldehyde interaction in a homogeneous system. *International Journal of*
845 *Biological Macromolecules*, *26*, 119–128. https://doi.org/10.1016 / s0141-8130
846 (99) 00068-9
847 Nazeer, M. A., Yilgör, E., & Yilgör, I. (2017). Intercalated chitosan/hydroxyapatite
848 nanocomposites: Promising materials for bone tissue engineering applications.
849 *Carbohydrate Polymers*, *175*, 38–46. https://doi.org/10.1016/j.carbpol.2017.07.054
850 Nick, C., Stuart, G., Jonathan, C., Nick, G., & Stuart, W. (2012). Organic Chemistry. In
851 *Oxford University Press Inc., New York* (2nd ed.). Oxford University Press Inc.
852 Park, S., & Lee, W. (2018). Removal of selected pharmaceuticals and personal care
853 products in reclaimed water during simulated managed aquifer recharge. *Science of*
854 *the Total Environment*, *640–641*, 671–677.
855 https://doi.org/10.1016/j.scitotenv.2018.05.221
856 Pinto, M. L., Mafra, L., Guil, J. M., Pires, J., & Rocha, J. (2011). Adsorption and
857 Activation of CO 2 by Amine-Modified Nanoporous Materials Studied by Solid-

State NMR and 13 CO 2 Adsorption. *Chemistry of Materials*, *23*(6), 1387–1395. https://doi.org/10.1021/cm1029563

Poon, L., Wilson, L. D., & Headley, J. V. (2014). Chitosan-glutaraldehyde copolymers and their sorption properties. *Carbohydrate Polymers*, *109*, 92–101. https://doi.org/10.1016/j.carbpol.2014.02.086

Pratt, D. Y., Wilson, L. D., & Kozinski, J. A. (2013). Preparation and sorption studies of glutaraldehyde cross-linked chitosan copolymers. *Journal of Colloid and Interface Science*, *395*(1), 205–211. https://doi.org/10.1016/j.jcis.2012.12.044

Ramachandran, S., Nandhakumar, S., & Dhanaraju, M. D. (2011). Formulation and characterization of glutaraldehyde cross-linked chitosan biodegradable microspheres loaded with famotidine. *Tropical Journal of Pharmaceutical Research*, *10*(3), 309–316. https://doi.org/10.4314/tjpr.v10i3.13

Riegger, B. R., Bäurer, B., Mirzayeva, A., Tovar, G. E. M., & Bach, M. (2018). A systematic approach of chitosan nanoparticle preparation via emulsion crosslinking as potential adsorbent in wastewater treatment. *Carbohydrate Polymers*, *180*, 46–54. https://doi.org/10.1016/j.carbpol.2017.10.002

Rogina, A., Ressler, A., Mati, I., Gallego Ferrer, G., Marijanovi, I., Ivankovi, M., & Ivankovi, H. (2017). Cellular hydrogels based on pH-responsive chitosan-hydroxyapatite system. *Carbohydrate Polymers*, *166*, 173–182. https://doi.org/10.1016/j.carbpol.2017.02.105

Rui, L., Xie, M., Hu, B., Zhou, L., Saeeduddin, M., & Zeng, X. (2017). Enhanced solubility and antioxidant activity of chlorogenic acid-chitosan conjugates due to the conjugation of chitosan with chlorogenic acid. *Carbohydrate Polymers*, *170*, 206–216. https://doi.org/10.1016/j.carbpol.2017.04.076

Salehi, E., Daraei, P., & Arabi Shamsabadi, A. (2016). A review on chitosan-based adsorptive membranes. *Carbohydrate Polymers*, *152*, 419–432. https://doi.org/10.1016/j.carbpol.2016.07.033

Sanchez, A. G., Prokhorov, E., Luna-barcenas, G., Mora-García, A. G., Kovalenko, Y., Miñoz, E. M. R., … Kovalenko, Y. (2018). Chitosan-hydroxyapatite nanocomposites: effect of interfacial layer on mechanical and dielectric properties. *Materials Chemistry and Physics*, *217*, 151–159. https://doi.org/10.1016/j.matchemphys.2018.06.062

Sathishkumar, P., Meena, R. A. A., Palanisami, T., Ashokkumar, V., Palvannan, T., & Gu, F. L. (2020). Occurrence, interactive effects and ecological risk of diclofenac

892 in environmental compartments and biota - a review. *Science of The Total*
893 *Environment*, *698*, 134057. https://doi.org/10.1016/j.scitotenv.2019.134057
894 Shariatinia, Z., & Jalali, A. M. (2018). Chitosan-based hydrogels: Preparation,
895 properties and applications. *International Journal of Biological Macromolecules*,
896 *115*, 194–220. https://doi.org/10.1016/j.ijbiomac.2018.04.034
897 Shi, C., Lv, C., Wu, L., & Hou, X. (2017). Porous chitosan/hydroxyapatite composite
898 membrane for dyes static and dynamic removal from aqueous solution. *Journal of*
899 *Hazardous Materials*, *338*, 241–249. https://doi.org/10.1016/j.jhazmat.2017.05.022
900 Silva, O. G., Alves, M. M., dos Santos, I. M. G., Fonseca, M. G., & Jaber, M. (2017).
901 Mesoporous calcium phosphate using casein as a template: Application to bovine
902 serum albumin sorption. *Colloids and Surfaces B: Biointerfaces*, *158*, 480–487.
903 https://doi.org/10.1016/j.colsurfb.2017.07.011
904 Soares, F. S., Fernandes, T., Sacramento, M., Trindade, T., & Daniel-da-silva, A. L.
905 (2019). Magnetic quaternary chitosan hybrid nanoparticles for the e ffi cient uptake
906 of diclofenac from water. *Carbohydrate Polymers*, *203*, 35–44.
907 https://doi.org/10.1016/j.carbpol.2018.09.030
908 Sousa, J. C. G., Ribeiro, A. R., Barbosa, M. O., Pereira, M. F. R., & Silva, A. M. T.
909 (2018). A review on environmental monitoring of water organic pollutants
910 identified by EU guidelines. *Journal of Hazardous Materials*, *344*, 146–162.
911 https://doi.org/10.1016/J.JHAZMAT.2017.09.058
912 Sun, K., Shi, Y., Wang, X., & Li, Z. (2017). Sorption and retention of diclofenac on
913 zeolite in the presence of cationic surfactant. *Journal of Hazardous Materials*, *323*,
914 584–592. https://doi.org/10.1016/J.JHAZMAT.2016.08.026
915 Szcześ, A., Hołysz, L., & Chibowski, E. (2017). Synthesis of hydroxyapatite for
916 biomedical applications. *Advances in Colloid and Interface Science*, *249*, 1–10.
917 https://doi.org/10.1016/j.cis.2017.04.007
918 Triebskorn, R., Berg, K., Ebert, I., Frey, M., Jungmann, D., Oehlmann, J., … Köhler, H.
919 R. (2015). Monitoring primary effects of pharmaceuticals in the aquatic
920 environment with mode of action-specific in vitro biotests. *Environmental Science*
921 *and Technology*, *49*(5), 2594–2595. https://doi.org/10.1021/acs.est.5b00162
922 Vakili, M., Deng, S., Li, T., Wang, W., Wang, W., & Yu, G. (2018). Novel crosslinked
923 chitosan for enhanced adsorption of hexavalent chromium in acidic solution.
924 *Chemical Engineering Journal*, *347*, 782–790.
925 https://doi.org/10.1016/J.CEJ.2018.04.181

926 Vakili, M., Rafatullah, M., Salamatinia, B., Abdullah, A. Z., Ibrahim, M. H., Tan, K. B.,
927 … Amouzgar, P. (2014). Application of chitosan and its derivatives as adsorbents
928 for dye removal from water and wastewater: A review. *Carbohydrate Polymers*,
929 *113*, 115–130. https://doi.org/10.1016/j.carbpol.2014.07.007
930 Venkatesan, J., Anil, S., Kim, S. K., & Shim, M. S. (2017). Chitosan as a vehicle for
931 growth factor delivery: Various preparations and their applications in bone tissue
932 regeneration. *International Journal of Biological Macromolecules*, *104*, 1383–
933 1397. https://doi.org/10.1016/j.ijbiomac.2017.01.072
934 Wang, Q., Li, J., Xu, T., Lu, X., Zhi, W., & Weng, J. (2017). Porous hydroxyapatite
935 scaffolds containing dual microspheres based on poly(lactide-co-glycolide) and
936 chitosan for bone regeneration. *Materials Letters*, *188*, 387–391.
937 https://doi.org/10.1016/j.matlet.2016.11.098
938 Wilson, L. D., & Xue, C. (2013). Macromolecular sorbent materials for urea capture.
939 *Journal of Applied Polymer Science*, *128*(1), 667–675.
940 https://doi.org/10.1002/app.38247
941 Yang, R., Li, H., Huang, M., Yang, H., & Li, A. (2016). A review on chitosan-based
942 flocculants and their applications in water treatment. *Water Research*, *95*, 59–89.
943 https://doi.org/10.1016/J.WATRES.2016.02.068
944 Ziegler-Borowska, M., Chełminiak, D., Kaczmarek, H., & Kaczmarek-Kędziera, A.
945 (2016). Effect of side substituents on thermal stability of the modified chitosan and
946 its nanocomposites with magnetite. *Journal of Thermal Analysis and Calorimetry*,
947 *124*(3), 1267–1280. https://doi.org/10.1007/s10973-016-5260-x
948 Zima, A. (2018). Spectrochimica Acta Part A : Molecular and Biomolecular
949 Spectroscopy Hydroxyapatite-chitosan based bioactive hybrid biomaterials with
950 improved mechanical strength. *Spectrochimica Acta Part A: Molecular and*
951 *Biomolecular Spectroscopy*, *193*, 175–184.
952 https://doi.org/10.1016/j.saa.2017.12.008
953